Research Article

Xiaoli Sun, Yuanyuan Wang, Bingzheng Yan, Kejian Yang, Wei Wei*, Ying Dai, Feng Chen, Baitao Zhang* and Jingliang He

Stoichiometric modulation on optical nonlinearity of 2D MoS$_x$Se$_{2−x}$ alloys for photonic applications

Abstract: The composition-engineered band structures of two-dimensional (2D) ternary transition-metal dichalcogenides (TMDCs) semiconductor alloys directly dominate their electronic and optical properties. Herein, in this paper, a detailed theoretical and experimental study on the composition-dependent nonlinear optical properties of 2D MoS$_x$Se$_{2−x}$ alloys was carried out. The first-principles calculations were performed to investigate the compositionally modulated properties of monolayer 2D MoS$_x$Se$_{2−x}$ (x = 0.25, 0.5, 1.0, 1.5, and 1.75) in terms of the carrier effective mass, carrier density and mobility, as well as band-gaps. Furthermore, high-quality few-layered MoS$_x$Se$_{2−x}$ (x = 0.2, 0.5, 1.0, 1.5, and 1.8) nanosheets were fabricated by using liquid phase exfoliation method. The third-order nonlinear optical response was investigated by open-aperture Z-scan technique, revealing composition-dependent saturable absorption, and light modulation properties, which were correlated to the theoretical calculations and further confirmed by using MoS$_x$Se$_{2−x}$ nanosheets as saturable absorbers (SAs) for all-solid-state pulsed lasers. In particular, a mode-locked solid-state laser with pulse width of 227 fs was realized with MoS$_{0.2}$Se$_{1.8}$ as SA, for the first time to our best knowledge. Our work not only provides a comprehensive understanding of the compositionally and defectively modulated nonlinear optical responses of ternary TMDCs alloys, but also paves a way for the development of 2D materials-based novel optoelectronic devices.

Keywords: electronic band structures; MoSSe; nonlinear optical responses; ultrafast laser.

1 Introduction

Low-dimensional nanomaterials exhibit unique physical and chemical properties and functions that much differ from their bulk counterparts due to the quantum confinement effect. Since the first discovery of graphene in 2004 [1], the research on two-dimensional (2D) layered materials beyond graphene has attracted significant attention and now been the hotspot of the frontier scientific research [2, 3]. In the past two decades, numerous efforts from both theories and experiments have been devoted to explore different kinds and properties of 2D layered materials [4–7]. Up to now, a variety of 2D layered materials have been reported, including hexagonal boron nitride (h-BN) [8], transition metal dichalcogenides (TMDCs, *e.g.*, MoS$_2$, WS$_2$, MoSe$_2$, etc.) [2, 3, 9], topological insulators (Bi$_2$Se$_3$, Bi$_2$Te$_3$, Sb$_2$Te$_3$, etc.) [10–12], black phosphorus (BP) [13, 14], transition metal carbides and carbonitrides (MXenes) [15], antimonene [16], and even mixed-dimensional van der Waals (vdW) heterostructures [17–19] etc. In particular, TMDCs semiconductors were discovered following behind graphene and have been regarded as the outstanding representative 2D materials because of their exotic and promising properties, including tunable band gap transiting from indirect of bulk to direct of monolayer, moderate carrier mobility, good bendability, and strong nonlinear optical response, making them to be exciting low-dimensional semiconductors for the new generation of electronic and photonic devices.

Since the electronic and optical properties of 2D semiconductors are strongly related to their band structures, band gap engineering plays a critical role in applications of electronics, photonics and optoelectronics and

*Corresponding authors: Wei Wei, School of Physics, Shandong University, Jinan 250100, China, E-mail: weiw@sdu.edu.cn; and
Baitao Zhang, State Key Laboratory of Crystal Materials, Institute of Novel Semiconductors, Shandong University, Jinan 250100, China, E-mail: btzhang@sdu.edu.cn. https://orcid.org/0000-0001-9105-0684 (B. Zhang)
Xiaoli Sun, Yuanyuan Wang, Ying Dai and Feng Chen, School of Physics, Shandong University, Jinan 250100, China
Bingzheng Yan, Kejian Yang and Jingliang He, State Key Laboratory of Crystal Materials, Institute of Novel Semiconductors, Shandong University, Jinan 250100, China. https://orcid.org/0000-0002-3937-0389 (B. Yan)

thus has become a significant research hotspot recently. It has been proved that the band gap of 2D TMDCs semiconductors can be tuned by thickness modulation [20], interface and defects engineering [21], gating effect [22], and formation of vdW heterostructures with different TMDCs [23, 24]. In addition, thanks to the similarities in the atomic structure of TMDCs materials (general formula MX_2 with M of a transition metal (groups IV, V, or VI) and X of a chalcogen (S, Se, or Te)), it is possible to create ternary TMDCs alloys with tunable band gaps by modulating the composition of M or X [25]. Up to now, a series of 2D TMDCs alloys such as MoS_xSe_{2-x}, WS_xSe_{2-x}, $Mo_xW_{1-x}S$, PtSSe, et al., have been theoretically and experimentally studied [25–28]. Among them, MoS_xSe_{2-x} is the mostly studied TMDCs alloy [26, 29]. It has a triple-layered structure with hexagonal Mo layer sandwiched by S and Se layers with a lattice parameter of 3.25 Å, Mo–S and Mo–Se bond lengths of 2.42 and 2.52 Å [30], respectively. The comparable cohesive energy of $MoSe_2$ (–2.34 eV) and MoS_2 (–2.63 eV) can sufficiently guarantee the stability of MoS_xSe_{2-x} alloys [31]. The previous researches have proved that the band gap of monolayer MoS_xSe_{2-x} alloys can be tuned from 1.87 to 1.55 eV by increasing Se concentration [32]. Considering the strain and gap bowing effect, the band gap can be even reduced to ~0.5 eV [33]. What's more, discontinuity in the work functions of S and Se atomic layers can break the out-of-plane structural symmetry and gives rise to many exotic physical properties [34]. The novel structure of monolayer half-to-half MoSSe has been systematically explored by the first-principles calculations, revealing that MoSSe has unique electronic and optical properties in comparison to pristine $MoSe_2$ and MoS_2 [30, 32, 35], such as good catalytic performance, strong Rashba spin splitting, large piezoelectric effect, and so on. The work function of MoS_xSe_{2-x} alloy and the carrier effective mass can be easily tuned by changing Se or S concentration, resulting in tunable carrier mobility and thus enhancing the performances of TMDCs semiconductors in electronic and photonic devices. Moreover, both binary and ternary 2D TMDCs semiconductors, e.g. MoS_2, $MoSe_2$, as well as MoSSe alloy nanosheets, have proved to exhibit nonlinear saturable absorption properties due to the Pauli blocking effect, and have been used for pulsed laser generation [9, 36, 37]. In generally, compared with the monolayer TMDs, few-layered TMDs have the stronger optical absorption and modulation ability [38]. However, the systematically study of MoS_xSe_{2-x} alloys with S concentration-dependent properties in terms of the band gap, the carrier effective mass, the carrier density and mobility, as well as the saturable absorption properties have rarely reported.

In this work, the band structure, carrier effective mass, carrier density and mobility, as well as band gaps of monolayer MoS_xSe_{2-x} alloys with S concentrations of $x = 0.25$, 0.5, 1.0, 1.5 and 1.75 were systematically studied by performing the first-principles calculations. Then, by using the liquid phase exfoliation (LPE) and spin-coating methods, the high-quality few-layered 2D MoS_xSe_{2-x} nanosheets with $x = 0.2$, 0.5, 1.0, 1.5 and 1.8 were successfully fabricated. The open-aperture Z-scan measurements at 1.06 μm were used to explore the saturable absorption properties of the as-prepared MoS_xSe_{2-x} nanosheets, demonstrating that the modulation parameters could be effectively tuned by varying S concentration x. Furthermore, the concentration-dependent modulation properties were further demonstrated by passively Q-switched Nd:YVO$_4$ lasers with 2D MoS_xSe_{2-x} ($x = 0.2$, 0.5, 1, 1.5 and 1.8) nanosheets-based saturable absorbers (SAs). In particular, a passively mode-locked Yb:KYW bulk laser with pulse width as short as 227 fs was realized with 2D $MoS_{0.2}Se_{1.8}$ nanosheets SA for the first time, to the best our knowledge. Our results provide a promising solution for the development of 2D TMDCs material-based electronic and photonic devices with desirable properties.

2 Results and discussion

2.1 Theoretical calculations

Based on density functional theory (DFT), we calculated the electronic band structures of monolayer MoS_xSe_{2-x} ($x = 0.25$, 0.5, 1.0, 1.5, and 1.75) alloys, results are shown as Figure S1. The calculation details were described in the Experimental Section. The intrinsic carrier density of a 2D semiconductor can be expressed as [39]:

$$n_i = g_{2D}k_BT \ln\left[1 + \exp\left(\frac{E_0}{-k_BT}\right)\right], g(E) = \frac{g_sg_vm^*}{2\pi\hbar^2} \quad (1)$$

where g_s and g_v are the spin and valley degeneracy factors, respectively; k_B is the Boltzmann's constant, m^* is the band-edge effective mass; $E_0 = E_g/2$, and E_g is the bandgap energy; T represents the temperature and is set to 300 K. Generally, for most 2D semiconductors, $E_0 \gg k_BT$, thus n_i can be approximated as [39]:

$$n_i \approx g_{2D}k_BT \exp\left(-\frac{E_g}{2k_BT}\right) \quad (2)$$

The carrier mobility can be calculated by the following equation [40, 41]:

$$\mu_{2D} = \frac{e\langle\tau\rangle}{m} = \frac{e\hbar^3 \rho S_1^2}{k_B T m_e^* m_d (E_i)^2}, m_d = \sqrt{m_x m_y} \qquad (3)$$

where e is the elementary charge, τ is the carrier relaxation time, ρ is the mass density, m is the carrier effective mass, m_e^* is the effective mass along the transport direction, and m_d is the equivalent density-of-state mass. The mass m_e^* and sound velocity S_l can be calculated in terms of the phonon $\omega(k)$ and electronic dispersion relations $E(k)$ with the following formulas:

$$S_l = \left[\frac{\partial\omega(k)}{\partial k}\right], m_e = \hbar\left[\frac{\partial^2 E(k)}{\partial k^2}\right]^{-1} \qquad (4)$$

E_1 is the deformation potential, defined as the energy shift of the bottom of the conduction band (CB) δE with the lattice deformation caused by phonons multiplying the lattice constant with a step of 0.5%. To reduce the computational burden, we chose five kinds of potential MoS_xSe_{2-x} alloys with S stoichiometric concentration $x = 0.25, 0.5, 1.0, 1.5,$ and 1.75.

It is obvious that all the structures show direct band gap of 1.46, 1.48, 1.55, 1.60, and 1.64 eV for $x = 0.25, 0.5, 1.0, 1.5,$ and 1.75, respectively. The relaxation time, carrier density and mobility of the 2D semiconductors dominate their free carrier optical absorption and nonlinear optical absorption responses, especially for the modulation depth and saturation intensity [42, 43]. The effective mass, carrier density, and mobility of electrons and holes along Γ-X(y) and X-S(x) directions were calculated and summarized Table S1. Figure 1(a) shows the electron mobility and effective mass as a function of x. The effective mass m^* decreases from 0.553 to 0.485 along zigzag direction (and 0.55 to 0.489 along armchair) as x increases from 0.25 to 1.75. According to Eq. (3), the carrier mobility is mainly determined by the carrier relaxation time and effective mass. In our calculations, the difference in the relaxation time between different MoS_xSe_{2-x} alloys is negligible since S and Se atoms have the similar electron distributions and

the lattice of different MoS_xSe_{2-x} alloys changes slightly. Therefore, the carrier mobility depends only on the effective mass. As S concentration increases, the electron mobility increases from 112.11 to 141.73 $cm^2 V^{-1} s^{-1}$ along zigzag direction, as shown in Figure 1(a). The variation of hole mobility and effective mass shows a similar trend to that of electron, see Figure 1(b). The hole mobility ranges from 509.20 to 798.91 $cm^2 V^{-1} s^{-1}$ with S concentration increases. According to Eq. (1), the intrinsic carrier density is closely related to the effective mass and band gap. As shown in Figure 1(d), the carrier density decreases as x increases, meaning that the free carrier optical absorption would be modulated by controlling x. It should be pointed out that the spin–orbit coupling (SOC) effect is also considered in the calculation [44, 45], which leads to Zeeman splitting at VBM and CBM. However, this splitting didn't change the effect of S/Se ratio on carrier mobility. Figure 1(c) summarizes the carrier mobility and carrier effective mass of TMDCs materials. Overall, according to the calculated results, it is obvious that the effective mass, carrier mobility and carrier concentration could be tuned *via* changing the nonmetal element composition.

2.2 Material fabrication and characterization

2D ternary TMDCs alloys with different S (or Se) atom concentrations have been successfully fabricated by using chemical vapor deposition (CVD) and exfoliation methods [4]. Here, in our experiment, we firstly synthesized MoS_xSe_{2-x} compounds powders with several S concentration and then exfoliated them into 2D nanosheets with LPE method. The detailed fabrication process is schematically shown in Figure S2. Sapphire and dielectric mirrors (coated for high reflection at 1020–1100 nm) were chosen as the substrates for performing the following measurements and experiments.
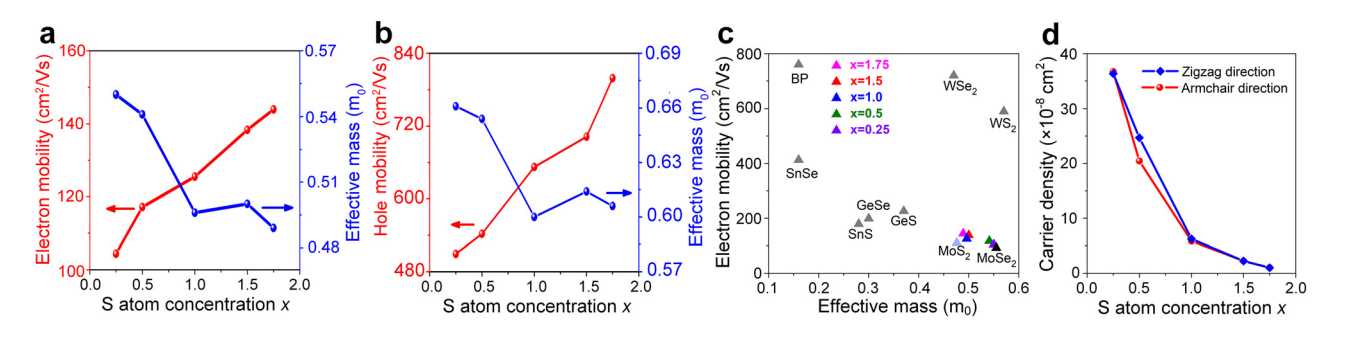

Figure 1: The calculated carrier parameters of MoS_xSe_{2-x}.
(a) Electron mobility and effective mass as a function of S concentration x. (b) Hole mobility and effective mass as a function of S concentration x. (c) Summary of the electron mobility and effective mass of 2D TMDCs semiconductors [46, 47]. (d) Carrier concentration along the armchair and zigzag directions as a function of S concentration x.

X-ray photoelectron spectroscopy (XPS) was employed to investigate the stoichiometric concentration (atomic ration) and binding energies of the as-prepared MoS_xSe_{2-x} nanosheets. Figure 2(a)–(c) show the characteristic spectra of Mo 3d, S 2p, S 2s, Se 3p, Se 3d for the prepared MoS_xSe_{2-x} alloys with different x. Considering the relative symmetric factors (R.S.F) for S $2p_{3/2}$ (0.849) and Se $3P_{3/2}$ (0.445), the quantitative atomic ratios of S and Se in MoS_xSe_{2-x} alloys were determined to be 1:8.96, 1:3.07, 1:1.2, 3.10:1, and 9.23:1 based on the formula:

$$S/Se = (I_S F_S)/(I_{Se} F_{Se}) \qquad (5)$$

where $I_S(I_{Se})$ and $F_S(F_{Se})$ represent the areas of the peaks and the R.S.F of S 2p (Se 3d) [48], respectively. In order to show the change of element composition more clearly, the values of x were determined to be rounded. Therefore, the corresponding S concentration x could be determined to be x = 0.2, 0.5, 1.0, 1.5, and 1.8, correspondingly. The energy dispersive X-ray spectroscopy (EDX) were measured for comparison, and the quantitative results agreed well with XPS results by considering the inevitable impurities or defects, as shown in Figure S3(a)–(e). Both the XPS and EDX results not only give a conclusion that the S concentrations (the value of x) of the as-prepared MoS_xSe_{2-x} alloys were 0.2, 0.5, 1.0, 1.5, and 1.8, but also verify the good sample quality.

From Figure 2(b) and (c), it is obvious that the intensity of S 2p peaks (S $2p_{3/2}$ at ~162.3 eV and S $2p_{1/2}$ at ~163.5 eV) increases as x increases, while Se 3p (Se $3p_{3/2}$ at ~161 eV and Se $3p_{1/2}$ at ~167 eV) and Se 3d (Se $3d_{5/2}$ at ~54.9 eV and Se $3d_{3/2}$ at ~55.7 eV) peaks intensity decreases. The variation trend is consistent with the previous report [49], while the corresponding binding energies are a little larger than those reported in refer [49], which might because of the thicker samples we used (monolayer in ref.). Figure 2(d)–(f) show the binding energy of Mo 3d, S 2p, and Se 3d as a function of x. As shown in Figure 2(d), it is noteworthy that the Mo $3d_{5/2}$ and Mo $3d_{3/2}$ shift to higher binding energy values as x increases. This is because the Mo 3d binding energy of MoS_2 ($3d_{5/2}$ of 229.6 eV and $3d_{3/2}$ of 232.8 eV) is larger than that of $MoSe_2$ ($3d_{5/2}$ of 228.3 eV and $3d_{3/2}$ of 231.5 eV) [50].

The surface morphologies of the as-prepared 2D MoS_xSe_{2-x} nanosheets were examined by atomic force microscopy (AFM) and scanning electron microscopy (SEM) measurements. Figure S4(a)–(e) show the topographic morphology of the MoS_xSe_{2-x} alloys with different S concentrations, respectively. The corresponding distributions of the nanosheets thickness are summarized and shown in Figure S4(f)–(j). The thickness of the as-prepared 2D MoS_xSe_{2-x} nanosheets with x = 0.2, 0.5, 1.0, 1.5, and 1.8 are all about ~8–11 nm (~90%), corresponding to the layer number of ~11–15. From the AFM results, the surface morphologies of the as-prepared 2D MoS_xSe_{2-x} nanosheets with different S concentrations are almost the same.
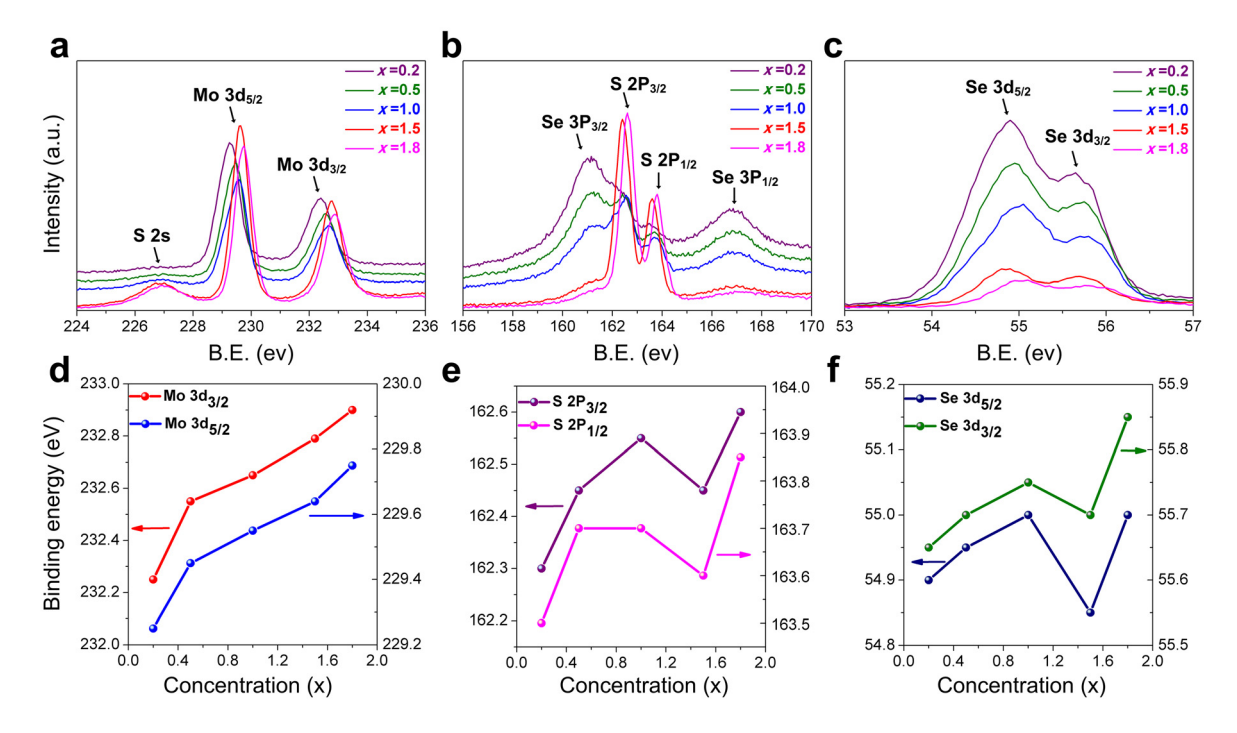

Figure 2: XPS spectra of (a) Mo 3d, (b) S 2p, and (c) Se 3d regions corresponding to MoS_xSe_{2-x} with different x values. (d)–(f) Plots of binding energy of the primary characteristic peaks as function of x.

$MoS_xSe_{2−x}$ sample with $x = 0.5$ was chosen as the representative for SEM and transmission electron microscopy (TEM) measurements. Figure 3(a) shows the typical SEM image with an irregular-shape sheet-like morphology, indicating the lateral size in order of micrometers. Combined with the TEM image shown in Figure 3(b), it is obvious that $MoS_xSe_{2−x}$ alloys are successfully exfoliated into few-layered structure. High resolution TEM (HRTEM) image taken from the edge of the nanosheets is shown in Figure 3(c), exhibiting a single-crystalline nature of the 2D vdW structures. The lattice space was measured to be 2.81 Å corresponding to the (100) plane of hexagonal $MoS_{0.5}Se_{1.5}$ (JCPDF no.36-1410) by amplifying the selected dotted box as shown in the inset of Figure 3(c). Figure 3(d) shows the selected area electron diffraction (SAED) pattern of the nanosheet, clearly defining single set of six-fold diffraction spots further demonstrated the high-quality hexagonal symmetry structures of the fabricated $MoS_xSe_{2−x}$ nanosheets [26], which matched well with the fast Fourier transform (FFT) results shown in Figure 3(e). Figure 3(f) depicts the 2D elemental mapping for the detected elements of Mo, S and Se, respectively in a selected region marked with a white rectangle, indicating that Mo, S and Se are uniformly and homogeneously distributed across the selected region.

Raman spectrum was used to characterize the composition-dependent vibration modes of the prepared 2D $MoS_xSe_{2−x}$ nanosheets. Figure 4(a) shows the normalized Raman spectra (excited by a 633 nm laser) of the as-prepared $MoS_xSe_{2−x}$ nanosheets. It can be clearly seen that there are two parts among the low wave number region (200–500 $cm^{−1}$): one is Mo–S related modes (A_{1g}(S–Mo), E_{2g}(S–Mo)) and the other one is Mo–Se related modes (A_{1g}(Se–Mo), E_{2g}(Se–Mo)). The intensities of Mo–Se related modes decrease with the increase of x, while the intensities of Mo–S related modes increase. Both the Mo–S and Mo–Se related modes shift to higher frequency as x increases. The slightly splitting might due to the variation in the coordination environment of Mo, which can be attributed to the substitution of heavy Se atoms with light S atoms. The variation of molecular vibration modes reveals good agreements with the gradually decreased (or increased) S (or Se) concentration in these compositionally modulated MoS_x-$Se_{2−x}$ alloys, which is in line with previous reports [26, 51, 52].

2D $MoS_xSe_{2−x}$ semiconductors have been proved to exhibit thickness dependent, compositionally and defectively modulated band structures [9]. The bandgap decreases as the thickness incereseas. In order to simplified computation, we calculated the electronic band structures of the few-layered $MoS_xSe_{2−x}$ nanosheets with $x = 0.25$, 0.5, 1.0, 1.5, and 1.75 by considering the S concentrations x as well as the Se vacancy defects (EDX results we measured). The EDX results (see Figure S3) demonstrate the existence of Se vacancy defects in our $MoS_xSe_{2−x}$ samples. As shown in Figure S5, unlike intrinsic materials, all the band structures show the indirect band gaps with different
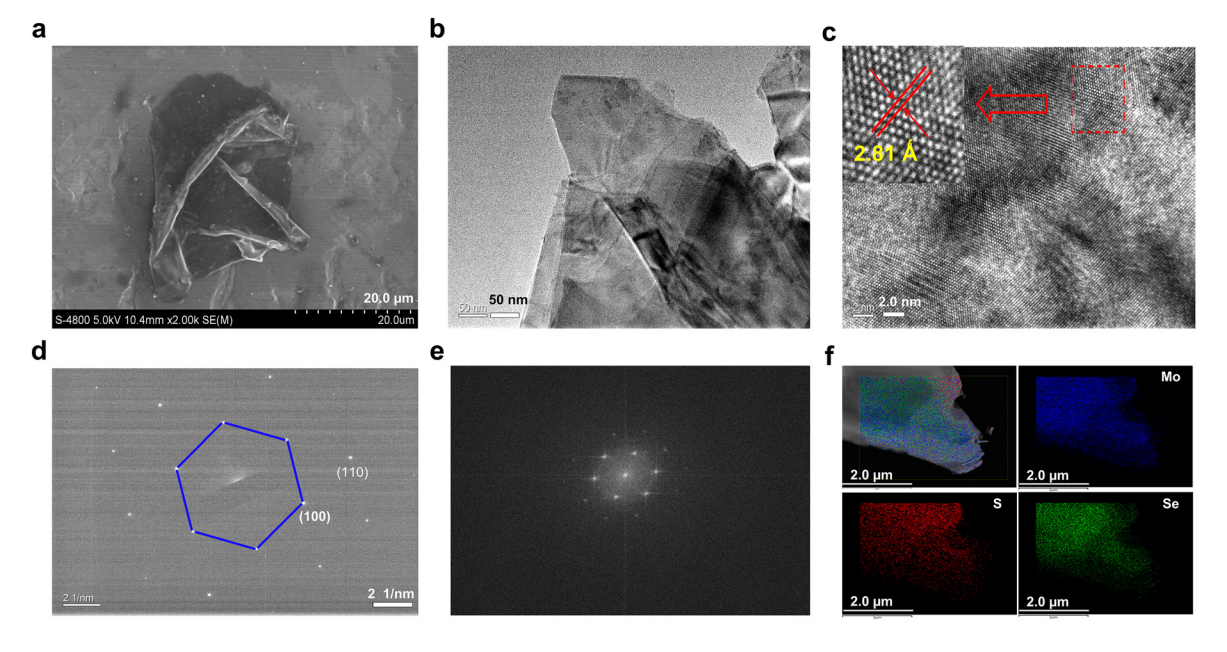

Figure 3: The morphology of sample. (a) SEM image of the surface of deposited $MoS_{0.5}Se_{1.5}$ alloy nanosheets. (b) Low and (c) high resolution TEM of $MoS_{0.5}Se_{1.5}$ alloy film, inset is the magnified crystal structure view of selected red box in (c). (d) The corresponding SAED patterns and (e) FFT image. (f) EDS elemental mapping of Mo, S and Se.
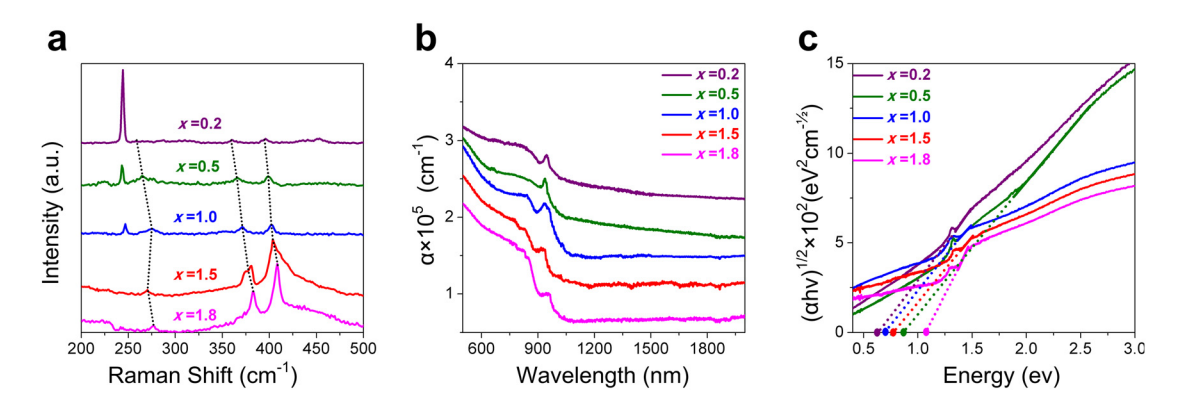
Figure 4: The Raman and linear absorption measurements.
(a) Raman spectra of MoS_xSe_{2-x} alloys with S composition x from 0.2 to 1.8. (b) UV-VIS-NIR absorption coefficient for the MoS_xSe_{2-x} with various S/Se ratios. (c) The graph of $(\alpha h\nu)^{1/2}$ versus $h\nu$ of MoS_xSe_{2-x} (x = 0.2, 0.5, 1.0, 1.5 and 1.8).

concentrations without evident variation trend. It might due to that the band gap of MoS_xSe_{2-x} is not only related to composition but also has a close relationship with the thickness and imperfections. The band gaps of imperfect MoS_xSe_{2-x} decrease to ~0.8 eV. Figure 4(b) shows the UV-VIS-NIR absorption spectra of the prepared few-layered 2D MoS_xSe_{2-x} (x = 0.2, 0.5, 1.0, 1.5, and 1.8) nanosheets measured by a U-3500 Hitachi UV-VIS-NIR spectrophotometer. As x increases, the absorption coefficient decreases, which is consistent with the variation of carrier density. Based on the Tauc theory [53], the optical band gap can be extracted by plotting $(\alpha h\nu)^{1/2}$ as a function of photon energy $h\nu$ and fitting the linear portion to the intercept with indirect band gap, where α is the linear absorption coefficient. As shown in Figure 4(c), the band gaps of MoS_xSe_{2-x} alloys are determined to be 0.63, 0.86, 0.70, 0.77, and 1.06 eV for x values of 0.2, 0.5, 1.0, 1.5, and 1.8, respectively. Both the theoretical and experimental results indicate that the optical response of as-prepared 2D MoS_xSe_{2-x} nanosheets can extend to 1.0 μm.

2.3 Nonlinear saturable absorption properties

Pauli blocking effect, defined as that two identical electrons cannot fill the same state under intensive light (photon energy larger than band gap) irradiation, results in the bleaching of light absorption (i.e. saturable absorption) and dominates the working mechanism of 2D semiconductors-based saturable absorber (SA). It is the key element of passively Q-switched or mode-locked lasers for generating nanosecond, picosecond or even femtosecond laser pulses. A variety of 2D TMDCs semiconductors have been proved to exhibit saturable absorption properties and

successfully used in fiber or solid-stated lasers for pulsed laser generation [42, 54, 55]. Here, 2D MoS_xSe_{2-x} (x = 0.2, 0.5, 1.0, 1.5 and 1.8) nanosheets-based SA devices were fabricated by transferring them onto the sapphire and dielectric mirrors substrates. The open-aperture Z-scan measurement and transmittance intensity scan (TI-scan) method were employed to explore the nonlinear saturable absorption responses of the few-layered MoS_xSe_{2-x} nanosheets-based SAs. The experimental setups are shown in Figure S6. Figure 5(a)–(e) show the typical Z-scan curves of the 2D MoS_xSe_{2-x} nanosheets-based SAs with x = 0.2, 0.5, 1.0, 1.5, and 1.8, respectively. To eliminate the error caused by the inhomogeneous distribution of the sample, we randomly selected five positions for Z-scan measurements. The light transmittance of each sample increases as the sample moving to the beam waist (Z = 0), i.e., the incident light intensity increases, forming a transmission peak at the waist, which verifies that all the MoS_xSe_{2-x} samples exhibit obvious saturable absorption behavior. It should be noticed that the fitting data of $MoS_{1.8}Se_{0.2}$ is a little scattering comparing with others, which might due to the heterogeneity thickness distribution as shown in AFM results. Figure S7 shows the modulation depths and the saturable intensities of the 2D MoS_xSe_{2-x} nanosheets based-SAs with x = 0.2, 0.5, 1.0, 1.5, and 1.8 at the five different measured positions.

TI-scan measurements were employed to further demonstrate the saturable absorption properties. The measured TI-scan curves are listed in Figure 5(f)–(j) showing the typical saturable absorption behavior of all the samples. Based on nonlinear optics, the optical nonlinearities of 2D semiconductors are directly related to photogenerated carrier density. The nonlinear saturable absorption caused by Pauli blocking effect in 2D MoS_xSe_{2-x} can be described by the simple two-level SA model [56]:
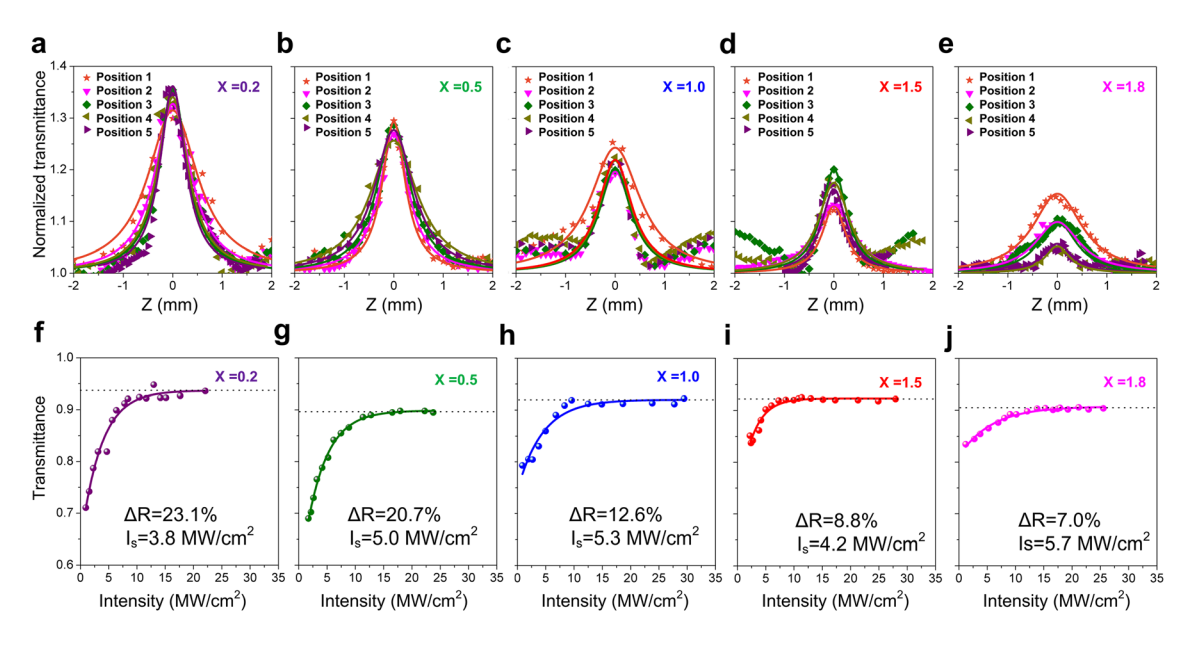
Figure 5: OA Z-scan measured curves of (a) $x = 0.2$, (b) $x = 0.5$, (c) $x = 1.0$, (d) $x = 1.5$ and (e) $x = 1.8$; TI-scan measured curves of (f) $x = 0.2$, (g) $x = 0.5$, (h) $x = 1.0$, (i) $x = 1.5$ and (j) $x = 1.8$.

$$\alpha^*(N) = \frac{\alpha_S^*}{1 + N/N_S} + \alpha_{NS}^* \qquad (6)$$

where $\alpha^*(N)$ is the nonlinear absorption coefficient, α_S^* and α_{NS}^* represent the saturable and nonsaturable absorption coefficient, respectively; N is the photogenerated carrier density and N_S is the saturation carrier density defined as the value of N when the absorption falls to one-half of the initial value. By introducing the incident laser intensity I and saturation intensity I_S to simplify the rate equation, N and N_S can be expressed as [56]:

$$N = \frac{\alpha^*(N)I\tau}{h\nu} \qquad (7)$$

$$N_S = \frac{\alpha^*(N)I_S\tau}{h\nu} \qquad (8)$$

Combining (6)–(8), the nonlinear saturable absorption can be rewritten as:

$$\alpha^*(I) = \frac{\alpha_S^*}{1 + \frac{I}{I_S}} + \alpha_{NS}^* \qquad (9)$$

Therefore, I_S is the key parameter to characterize the saturation performance of the photogenerated carriers during the saturable absorption process. When light propagates through a nonlinear optical material, the light attenuation can be expressed as:

$$\frac{dI}{dz} = -\alpha(I)I \qquad (10)$$

where z is the propagating distance in the material. With Eqs. (9) and (10), the nonlinear transmission curve can be described as [57, 58]:

$$T = A \exp\left(\frac{-\Delta R}{1 + \frac{I}{I_S}}\right) \qquad (11)$$

where A is a normalization constant, $\triangle R$ is the modulation depth. Using Eq. (11) to fit the nonlinear transmission curves, we can get the saturable absorption parameters in terms of modulation depth $\triangle R$, the saturation intensity I_S and the nonsaturable loss, which are listed in Table 1. As x increases from 0.2 to 1.8, the modulation depth decreases from 23.1 to 7.0%, while the saturation intensity increases from 3.8 to 5.7 MW cm^{-2}. The modulation depth of the 2D MoS$_x$Se$_{2-x}$ nanosheets is proportional to the carrier density, while the saturation intensity behaves oppositely [43, 59, 60]. Therefore, the larger carrier density indicates a higher modulation depth and lower saturation intensity. The variation trend of the saturable parameters is consistent with the theoretical results, i.e., the carrier density increases as S concentration decreases. The saturation intensity is one order of magnitude larger than that of graphene (0.61–0.71 MW cm^{-2}) [56], and three times greater than that of black phosphorus (1.35 MW cm^{-2}) [61], which indicates that the as-prepared 2D MoS$_x$Se$_{2-x}$ nanosheet-based SAs have excellent saturable absorption properties and quite suitable for passive Q-switching or mode-locking pulsed laser generation. Our

Table 1: Saturable absorption parameters of 2D MoS$_x$Se$_{2-x}$ nanosheets based-SAs.

Concentration	$x = 0.2$	$x = 0.5$	$x = 1.0$	$x = 1.5$	$x = 1.8$
Modulation depth	23.1%	20.7%	12.6%	8.8%	7.0%
Saturation intensity (MW/cm^2)	3.8	5.0	5.3	4.2	5.7
Nonsaturable loss	5.8%	10.1%	8.5%	7.2%	9.1%

Table 2: Summary of output parameters of the passively Q-switched Nd:YVO$_4$ lasers with 2D MoS$_x$Se$_{2-x}$ nanosheets based-SAs.

Sample MoS$_x$Se$_{2-x}$	Threshold (W)	Pulse width (ns)	Repetition rate (kHz)	Output power (mW)
$x = 0$	2.1	390	137.1	40
$x = 0.2$	1.5	552	146.2	45
$x = 0.5$	2.7	760	150.4	28
$x = 1$	1.9	940	133.4	52
$x = 1.5$	1.7	1190	143.4	60
$x = 1.8$	2.5	1240	137.8	47
$x = 2$	1.8	1337	118.5	37

results also suggest that it might be a new strategy to modulate the nonlinear response of 2D TMDCs alloy materials *via* tuning the element compositions.

2.4 Laser performance characterization

The modulation depth, saturable intensity, and nonsaturable loss are three key parameters of SA for passively Q-switched and mode-locked pulsed lasers. To validate the variation of the nonlinear saturable absorption parameters of 2D MoS$_x$Se$_{2-x}$ nanosheets-based SAs as a function of S concentration, a passively Q-switched Nd:YVO$_4$ laser was built. The experimental setup is schematically shown in Figure S8. Inserting the 2D MoS$_x$Se$_{2-x}$ nanosheets-based SAs into the laser cavity, the typical passively Q-switched lasers were realized. Table 2 summarizes the detailed output parameters (e.g., laser threshold, average output power, pulse duration, and repetition rate) of the passive Q-switching lasers. The thresholds of passively Q-switched lasers with MoS$_{0.5}$Se$_{1.5}$ and MoS$_{1.8}$Se$_{0.2}$ are slightly higher than those of others, which is due probably to the relative larger nonsaturable losses. The variations of the shortest pulse width and the largest repetition rates as a function of x are shown in Figure 6(a). The shortest pulse durations are determined to be 552, 760, 940, 1190, and 1240 ns for $x = 0.2$, 0.5, 1, 1.5, and 1.8, while the highest repetition rates are 146.2, 150.4, 133.4, 143.4, and 137.8 kHz, respectively. As x increases, the pulse width increases and the repetition rates hardly change. Considering the decrease in growth and decay of laser pulse during the gain saturation, the exact pulse duration can be expressed as [62]:

$$\Delta t \approx \frac{3.52 T_R}{\Delta R} \qquad (12)$$

where T_R is the cavity round-trip time. Note that Δt is inversely proportional to ΔR. Therefore, the variation trend of passively Q-switched pulse width well reflects that of the modulation depth, that is, the larger modulation depth, the shorter passive Q-switching pulse width would be

generated. The results of the passively Q-switched lasers further prove that the nonlinear optical parameters of 2D MoS$_x$Se$_{2-x}$ nanosheets could be tuned by changing the S (Se) concentration. Figure S9 shows the shortest pulse profiles and the corresponding pulse train obtained with MoS$_x$Se$_{2-x}$ SAs. It is obvious that the pulse train of MoS$_{0.2}$Se$_{1.8}$ is more stable. In order to compare the Q-switched laser performance, pure MoS$_2$ and MoSe$_2$ are employed as SA. The typical pulse train and temporal pulse profile were shown as Figure S10.

Passive mode-locking is a main technique for generating ultrafast pulsed lasers with the duration much shorter than that of passive Q-switching. In order to further characterize the potential of ternary 2D MoS$_x$Se$_{2-x}$ alloys in ultrafast laser generation, a 3.4-m-long Z-type mode-locking laser resonator was developed. The experimental setup is shown in Figure S11. It is much more difficult to realize a 2D material-based CW mode-locking operation than passive Q-switching operation for all solid-state lasers. Based on mode-locking theory, stable CW mode locking can only be realized when the mode-locking pulse energy E_p is greater than the minimum intracavity pulse energy $E_{p,c}$, which can be expressed by the following equation [63]:

$$F_{\text{sat, A}} \Delta R \Delta \frac{(PT_R)^2}{F_{\text{sat, L}} A_{\text{eff, L}} A_{\text{eff, A}}} = \frac{(PT_R)^2 \times m\sigma_{\text{em, L}}\lambda}{hc \times \pi\omega_{\text{eff, L}}^2 \times \pi\omega_{\text{eff, A}}^2} \qquad (13)$$

where $F_{\text{sat,A}}$ is the saturation fluence of the SA, P is the intracavity pulsed laser power, T_R is the round-trip time, $\omega_{\text{eff,A}}$ and $\omega_{\text{eff,L}}$ are the effective laser radii at the positions of the SA and laser crystal, $A_{\text{eff,A}}$ and $A_{\text{eff,L}}$ are the effective laser mode areas on the SA and laser crystal, $\sigma_{\text{em,L}}$ is the emission cross-section of the laser crystal, λ is the laser wavelength, h is the Planck constant, c is the light velocity, and m is a cavity constant with $m = 1$ for a ring cavity, and
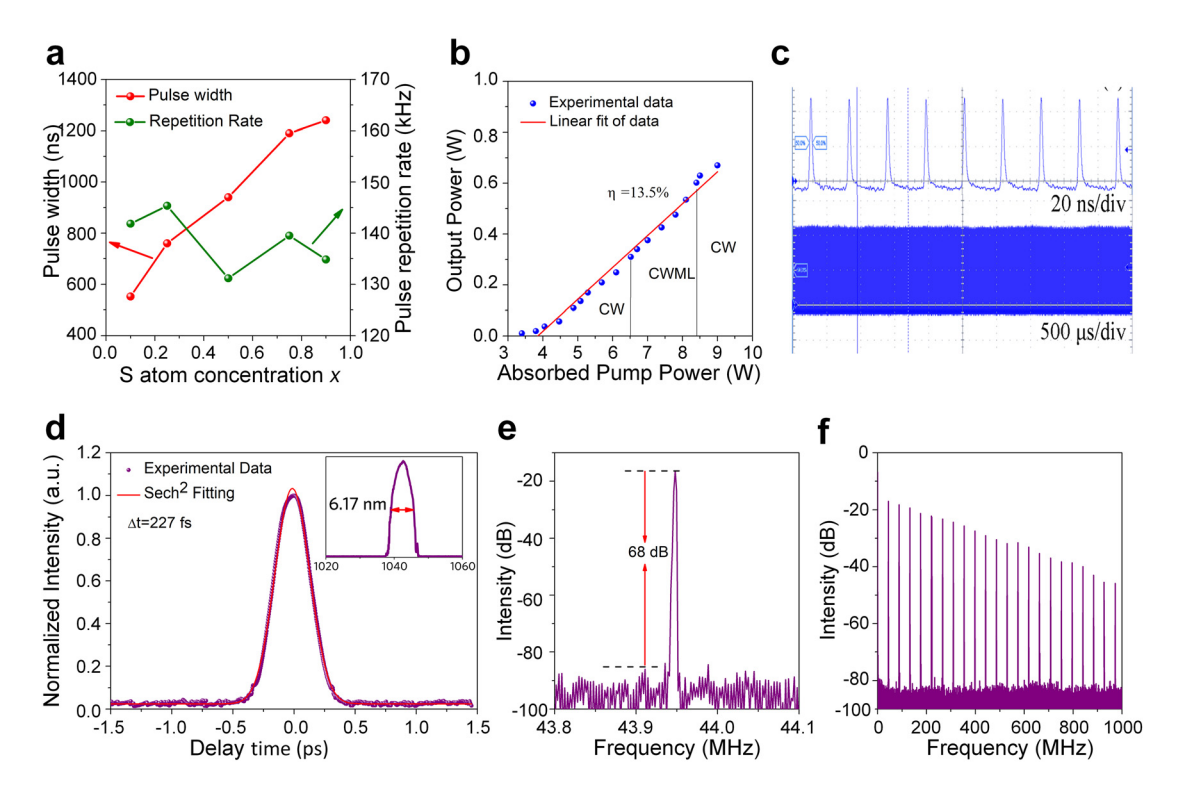
Figure 6: The CWML performance based on $MoS_{0.2}Se_{1.8}$ SA.
(a) Pulse width and repetition rate versus the composition x based Q-switched laser. (b) Average output power versus the absorbed pump of the $MoS_{0.2}Se_{1.8}$-based CWML laser. (c) Recorded typical pulse trains of CWML at the maximum output power. (d) Autocorrelation trace for 227 fs of CWML laser; inset is emission spectrum. Recorded frequency spectrum with a narrow (e) and a wide span (f).

$m = 2$ for a linear cavity. In addition, the pulse energy should be high enough to bleach the SA in order to benefit from the full modulation depth of SA in CWML lasers. In general, the intracavity pulse fluence on the SA must be approximately five times higher than the absorber saturation fluence [64]. Based on Eq. (13), considering the laser crystal properties, SA parameters and cavity design, we finally chose 2D $MoS_{0.2}Se_{1.8}$ nanosheets as the SA to realize the CW mode-locking (CWML) operation. In our experiment, the emission cross-section $\sigma_{em,L}$ of the laser crystal is 3.1×10^{-20} cm^2, and T_R, $\omega_{eff,A}$ and $\omega_{eff,L}$ turn out to be ~22.7 ns, 52 μm and 55 μm, respectively, corresponding to the laser cavity design. The left-hand side of Eq. (13), $F_{sat,A}\Delta R$, was calculated to be 13.2 μJ cm^{-2}, while the right-hand side was 67.43 μJ cm^{-2}. Therefore, stable CW mode-locked lasers can be obtained with the as-prepared 2D $MoS_{0.2}Se_{1.8}$ nanosheet SA and the as-designed laser cavity. It should be noticed that the as-prepared $MoS_{0.2}Se_{1.8}$ nanosheets was directly transferred onto a K9 dielectric mirror with high-reflection (HR) coating at 1020–1100 nm to fabricate the $MoS_{0.2}Se_{1.8}$ saturable absorption mirror (SAM). The 2D $MoS_{0.2}Se_{1.8}$ nanosheets here have the same morphology, thickness and therefore the

same saturable absorption properties as the one in the Z-scan measurement.

After inserting the $MoS_{0.2}Se_{1.8}$ SAM into the cavity, a CWML operation is achieved with careful adjustment. A pure K9 dielectric mirror with HR coating at 1020–1100 nm was used as the reference, with which the laser is operated in the continuously wave regime and no mode-locked phenomena can be observed. Figure 6(b) presents the variation between the average output power and the absorbed pump power of the $MoS_{0.2}Se_{1.8}$ SAM based mode-locking laser. The average output power is measured from both outputs. The CWML operation was started from the absorbed pump power of 6.5 W and could be sustained up to 8.4 W. The maximum average output power of the CWML operation is 0.62 W with a slope efficiency of 13.5%. The recorded maximum output power shows an instability of about ±3% for 1 h. We collect the CWML pulse trains in the maximum output power at different time scales, as shown in Figure 6(c). The period of the CWML output pulses is 22.7 ns, which is consistent with the round-trip time and the fundamental resonance frequency of the 3.4 m Z-type cavity length. The instability (output power, rms) was measured to

be less than 2.5% for 2 h. However, when increasing the absorbed pump power over than 8.4 W, the CWML state is broken due to the over-saturation of the SAM. At this point, no damage is observed in the surface of SAM.

At the maximum output power, we measured the pulse duration of the CWML laser by a commercial autocorrelator (APE, Pulse Check 150). Figure 6(d) shows the autocorrelation trace and the corresponding output spectrum (inset of Figure 6(d)) of the mode-locking laser pulse. Using a Sech^2 pulse shape fitting, the pulse width was determined to be 227 fs. The spectrum of CWML laser centered at 1042.5 nm with the FWHM of 6.17 nm, corresponding to the time bandwidth product of 0.386. What's more, the radio-frequency (RF) spectra at different spans were recorded by a spectrum analyzer (Agilent N9000A). As shown in Figure 6(e), a clear and sharp peak located at 43.94 MHz with the resolution bandwidth (RBW) of 2 kHz corresponding to the signal-to-noise ratio of 68 dB was observed. No spurious modulation signal exists in the RF spectra, proving clean CWML pulses based $MoS_{0.2}Se_{1.8}$ SAM have been achieved. To evaluate the stability of the CWML laser, a wide span of 1000 MHz with RBW of 110 kHz was recorded in Figure 6(f).

3 Conclusions

In summary, by performing the first-principles calculations, the S concentrations ($x = 0.25, 0.5, 1.0, 1.5$ and 1.75) dependent properties of monolayer 2D MoS_xSe_{2-x} alloys including the band gap, carrier effective mass, the carrier mobility and carrier concentrations were studied. By using LPE method, few layered 2D MoS_xSe_{2-x} nanosheets with S concentrations of $x = 0.2, 0.5, 1.0, 1.5$ and 1.8 were fabricated. The nonlinear saturable absorption responses were thoroughly explored by open-aperture Z-scan and TI-scan measurements, revealing the S concentration dependent saturable absorption properties, which are consistent with the theoretical calculations. By using 2D MoS_xSe_{2-x} nanosheets as SAs, passively Q-switched laser operation at $1.0\,\mu m$ band were realized, and results further confirm the S concentration dependent saturable absorption properties. Furthermore, by using $MoS_{0.2}Se_{1.8}$ SAM, CWML solid-state laser with the pulse as short as 227 fs and maximum output power of 0.62 W was demonstrated for the first time, indicating the potential of MoS_xSe_{2-x} alloys for ultrafast photonics application. Our work delivers a fresh insight into tailoring 2D alloys so as to develop desired photonic materials, which may find wide applications for pulse laser generation and all-optical signal processing.

4 Methods and experimental section

4.1 Density function theory calculation details

In this work, all calculations were performed by using the first-principles approach based on density functional theory (DFT) as implemented in Vienna ab-initio simulation package (VASP), and in conjunction with the projector augmented wave (PAW) method. The generalized gradient approximation (GGA) in the Perdew–Burke–Ernzerhof (PBE) form and a cutoff energy of 500 eV was applied to optimize the geometric structure of MoS_xSe_{2-x} alloys. A vacuum space of ≈20 Å along the direction normal to the monolayer plane was undertaken, which was sufficiently large to eliminate the interactions between two neighboring images caused by the periodic boundary condition. $2 \times 2 \times 1$ orthorhombic supercell, as shown as Figure S12, was used for geometric optimization and the carrier parameters calculation. A Monkhorst–Pack mesh of $7 \times 10 \times 1$ was used to sample the Brillouin zone. The criterion for the convergence of the force on each atom was set to be $0.01\,eV\,Å^{-1}$, and the total energy change was converged to be less than $1.0 \times 10^{-5}\,eV$. In addition, it should be point out that the carrier parameters of MoS_xSe_{2-x} alloys are not sensitive to the relative position of S and Se atoms, because these two elements belong to the same group. Therefore, in our calculation process, the S and Se atoms are evenly distributed on both sides of the supercell for MoSSe, which have different stoichiometry.

4.2 Experimental setup of Q-switched Nd:YVO$_4$ laser

The pump source is a fiber-coupled laser diode emitting at 808 nm. The fiber core is 400 μm in diameter with a numerical aperture (NA) of 0.22. Plane mirror M1 was antireflection coated at 808 nm and high-reflection coated at 1.06 μm. Concave mirror M2 with curvature radius of 40 mm was employed as an output coupling mirror with a transmission of 3% at 1.06 μm. The high-quality c-cut Nd:YVO$_4$ crystal with Nd-doping concentration of 0.3 at.% was wrapped in indium foil and tightly mounted in a copper block water-cooled to 18 °C. The pulse profiles and trains were recorded by a digital oscilloscope (1 GHz bandwidth, 5 Gs s^{-1} sampling rate, Tektronics DPO 7104) and an InGaAs fast photodetector (1 GHz bandwidth, New focus 1611).

4.3 Experimental setup of mode-locked Yb:KYW laser

A 10 at.% doped Np-cut 4-mm-long Yb:KYW crystal with right-angled cutting was chosen as the gain medium. A fiber-coupled diode laser emitting at 976 nm with a core diameter of 105 μm and a numerical aperture of 0.22 was used as the pump source. The pump spot was focused onto the laser crystal with a diameter of 58 μm by using a 1.8:1 optical coupling system. The pump laser beam matched well with the oscillate laser beam to ensure the fundamental laser mode output.

References

[1] K. S. Novoselov, A. K. Geim, S. V. Morozov, et al., "Electric field effect in atomically thin carbon films," *Science*, vol. 306, pp. 666–669, 2004.

[2] S. Manzeli, D. Ovchinnikov, D. Pasquier, O. V. Yazyev, and A. Kis, "2D transition metal dichalcogenides," *Nat. Rev. Mater.*, vol. 2, p. 17033, 2017.

[3] A. Gupta, T. Sakthivel, and S. Seal, "Recent development in 2D materials beyond graphene," *Prog. Mater. Sci.*, vol. 73, pp. 44–126, 2015.

[4] D. Chu and E. K. Kim, "Recent advances in synthesis and assembly of van der Waals materials," *J. Kor. Phys. Soc.*, vol. 73, pp. 805–816, 2018.

[5] Q. H. Wang, K. Kalantar-Zadeh, A. Kis, J. N. Coleman, and M. S. Strano, "Electronics and optoelectronics of two-dimensional transition metal dichalcogenides," *Nat. Nanotechnol.*, vol. 7, p. 699, 2012.

[6] J. He, L. Tao, H. Zhang, B. Zhou, and J. Li, "Emerging 2D materials beyond graphene for ultrashort pulse generation in fiber lasers," *Nanoscale*, vol. 11, pp. 2577–2593, 2019.

[7] X. Jiang, L. Zhang, S. Liu, et al., "Ultrathin metal-organic framework: an emerging broadband nonlinear optical material for ultrafast photonics," *Adv. Opt. Mater.*, vol. 6, p. 1800561, 2018.

[8] L. Liu, Y. P. Feng, and Z. X. Shen, "Structural and electronic properties ofh-BN," *Phys. Rev. B*, vol. 68, p. 104102, 2003.

[9] S. Wang, H. Yu, H. Zhang, et al., "Broadband few-layer MoS$_2$ saturable absorbers," *Adv. Mater.*, vol. 26, pp. 3538–3544, 2014.

[10] C.-Z. Chang, J. Zhang, X. Feng, et al., "Experimental observation of the quantum anomalous Hall effect in a magnetic topological insulator," *Science*, vol. 340, p. 167, 2013.

[11] B. A. Bernevig, T. L. Hughes, and S. C. Zhang, "Quantum spin Hall effect and topological phase transition in HgTe quantum wells," *Science*, vol. 314, p. 1757, 2016.

[12] X.-L. Qi, R. Li, J. Zang, and S.-C. Zhang, "Inducing a magnetic monopole with topological surface states," *Science*, vol. 323, p. 1184, 2009.

[13] L. Li, Y. Yu, G. J. Ye, et al., "Black phosphorus field-effect transistors," *Nat. Nanotechnol.*, vol. 9, p. 372, 2014.

[14] M. Zhang, Q. Wu, F. Zhang, et al., "Black-phosphorous-based pulsed lasers: 2D black phosphorus saturable absorbers for ultrafast photonics," *Adv. Opt. Mater.*, vol. 7, p. 1970001, 2019.

[15] K. Hantanasirisakul, M. Q. Zhao, P. Urbankowski, et al., "Fabrication of Ti$_3$C$_2$T$_x$ MXene transparent thin films with tunable optoelectronic properties," *Adv. Electron. Mater.*, vol. 2, p. 1600050, 2016.

[16] G. Zhang, X. Tang, X. Fu, et al., "2D group-VA fluorinated antimonene: synthesis and saturable absorption," *Nanoscale*, vol. 11, pp. 1762–1769, 2019.

[17] K. S. Novoselov, A. Mishchenko, A. Carvalho, and A. H. Castro Neto, "2D materials and van der Waals heterostructures," *Science*, vol. 353, p. 9439, 2016.

[18] D. Jariwala, T. J. Marks, and M. C. Hersam, "Mixed-dimensional van der Waals heterostructures," *Nat. Mater.*, vol. 16, p. 170, 2016.

[19] X. Sun, B. Zhang, Y. Li, et al., "Tunable ultrafast nonlinear optical properties of graphene/MoS$_2$ van der Waals heterostructures and their application in solid-state bulk lasers," *ACS Nano*, vol. 12, pp. 11376–11385, 2018.

[20] A. Splendiani, L. Sun, Y. Zhang, et al., "Emerging photoluminescence in monolayer MoS$_2$," *Nano Lett.*, vol. 10, pp. 1271–1275, 2010.

[21] Z. Hu, Z. Wu, C. Han, J. He, Z. Ni, and W. Chen, "Two-dimensional transition metal dichalcogenides: interface and defect engineering," *Chem. Soc. Rev.*, vol. 47, pp. 3100–3128, 2018.

[22] T. Jiang, D. Huang, J. Cheng, et al., "Gate-tunable third-order nonlinear optical response of massless Dirac fermions in graphene," *Nat. Photonincs*, vol. 12, pp. 430–436, 2018.

[23] Y. Gong, J. Lin, X. Wang, et al., "Vertical and in-plane heterostructures from WS$_2$/MoS$_2$ monolayers," *Nat. Mater.*, vol. 13, p. 1135, 2014.

[24] Y. Gong, S. Lei, G. Ye, et al., "Two-step growth of two-dimensional WSe$_2$/MoSe$_2$ heterostructures," *Nano Lett.*, vol. 15, pp. 6135–6141, 2015.

[25] R. Li, Y. Cheng, and W. Huang, "Recent progress of Janus 2D transition metal chalcogenides: from theory to experiments," *Small*, vol. 14, p. 1802091, 2018.

[26] H. Li, X. Duan, X. Wu, et al., "Growth of alloy MoS$_{2x}$Se$_{2(1-x)}$ nanosheets with fully tunable chemical compositions and optical properties," *J. Am. Chem. Soc.*, vol. 136, pp. 3756–3759, 2014.

[27] Q. Fu, L. Yang, W. Wang, et al., "Synthesis and enhanced electrochemical catalytic performance of monolayer $WS_{2(1-x)}Se_{2x}$ with a tunable band gap," *Adv. Mater.*, vol. 27, pp. 4732–4738, 2015.

[28] R. Peng, Y. Ma, B. Huang, and Y. Dai, "Two-dimensional Janus PtSSe for photocatalytic water splitting under the visible or infrared light," *J. Mater. Chem. A*, vol. 7, pp. 603–610, 2019.

[29] R. Peng, Y. Ma, S. Zhang, B. Huang, and Y. Dai, "Valley polarization in Janus single-layer MoSSe via magnetic doping," *J. Phys. Chem. Lett.*, vol. 9, pp. 3612–3617, 2018.

[30] W.-J. Yin, B. Wen, G.-Z. Nie, X.-L. Wei, and L.-M. Liu, "Tunable dipole and carrier mobility for a few layer Janus MoSSe structure," *J. Mater. Chem. C*, vol. 6, pp. 1693–1700, 2018.

[31] F. Li, W. Wei, P. Zhao, B. Huang, and Y. Dai, "Electronic and optical properties of pristine and vertical and lateral heterostructures of janus MoSSe and WSSe," *J. Phys. Chem. Lett.*, vol. 8, pp. 5959–5965, 2017.

[32] J. Mann, Q. Ma, P. M. Odenthal, et al., "2-Dimensional transition metal dichalcogenides with tunable direct band gaps: $MoS_{2(1-x)}Se_{2x}$ monolayers," *Adv. Mater.*, vol. 26, pp. 1399–1404, 2014.

[33] Y.-N. Wen, M.-G. Xia, and S.-L. Zhang, "Bandgap engineering of Janus MoSSe monolayer implemented by Se vacancy," *Comput. Mater. Sci.*, vol. 152, pp. 20–27, 2018.

[34] A.-Y. Lu, H. Zhu, J. Xiao, et al., "Janus monolayers of transition metal dichalcogenides," *Nat. Nanotechnol.*, vol. 12, p. 744, 2017.

[35] G. Bishal and R. Moradian, "Ab initio investigation of the optical properties of layered $MoS_xSe_{(2-x)}$ ($0 \leq x \leq 2$): by GGA and mBJ approaches," *Int. J. Mod. Phys. B*, vol. 33, p. 1950062, 2019.

[36] H. Jin, T. Wang, Z.-R. Gong, C. Long, and Y. Dai, "Prediction of an extremely long exciton lifetime in a Janus-MoSTe monolayer," *Nanoscale*, vol. 10, pp. 19310–19315, 2018.

[37] B. Z. Yan, B. T. Zhang, J. L. He, et al., "MoSSe saturable absorber based high-power passively Q-switched 2.0 μm bulk laser," *IEEE Photon. Technol. Lett.*, vol. 1, p. 1, 2019.

[38] N. Dong, Y. Li, S. Zhang, et al., "Saturation of two-photon absorption in layered transition metal dichalcogenides: experiment and theory," *ACS Photonics*, vol. 5, pp. 1558–1565, 2018.

[39] Ma N. and Jena D., "Carrier statistics and quantum capacitance effects on mobility extraction in two-dimensional crystal semiconductor field-effect transistors," *2D Mater.*, vol. 2, 2015, Art no. 015003.

[40] S. Bruzzone and G. Fiori, "Ab-initio simulations of deformation potentials and electron mobility in chemically modified graphene and two-dimensional hexagonal boron-nitride," *Appl. Phys. Lett.*, vol. 99, p. 222108, 2011.

[41] S. Takagi, A. Toriumi, M. Iwase, and H. Tango, "On the universality of inversion layer mobility in Si MOSFET's: Part I-effects of substrate impurity concentration," *IEEE Trans. Electron Dev.*, vol. 41, pp. 2357–2362, 1994.

[42] S. Wang, H. Yu, and H. Zhang, "Band-gap modulation of two-dimensional saturable absorbers for solid-state lasers," *Photon. Res.*, vol. 3, pp. A10–A20, 2015.

[43] W. Liu, Y.-N. Zhu, M. Liu, et al., "Optical properties and applications for MoS_2-Sb_2Te_3-MoS_2 heterostructure materials," *Photon. Res.*, vol. 6, p. 220, 2018.

[44] D. Xiao, G.-B. Liu, W. Feng, X. Xu, and W. Yao, "Coupled spin and valley physics in monolayers of MoS_2 and other group-VI dichalcogenides," *Phys. Rev. Lett.*, vol. 108, p. 196802, 2012.

[45] A. Molina-Sánchez, D. Sangalli, L. Wirtz, and A. Marini, "Ab initio calculations of ultrashort carrier dynamics in two-dimensional materials: valley depolarization in single-layer WSe_2," *Nano Lett.*, vol. 17, pp. 4549–4555, 2017.

[46] A. Shafique and Y.-H. Shin, "Thermoelectric and phonon transport properties of two-dimensional IV-VI compounds," *Sci. Rep.*, vol. 7, p. 506, 2017.

[47] J. Qiao, X. Kong, Z.-X. Hu, F. Yang, and W. Ji, "High-mobility transport anisotropy and linear dichroism in few-layer black phosphorus," *Nat. Commun.*, vol. 5, p. 4475, 2014.

[48] Z. Lin, B. Lin, Z. Wang, et al., "Facile preparation of 1T/2H-Mo$(S_{1-x}Se_x)_2$ nanoparticles for boosting hydrogen evolution reaction," *ChemCatChem*, vol. 11, pp. 2217–2222, 2019.

[49] Y. Gong, Z. Liu, A. R. Lupini, et al., "Band gap engineering and layer-by-layer mapping of selenium-doped molybdenum disulfide," *Nano Lett.*, vol. 14, pp. 442–449, 2014.

[50] V. Kiran, D. Mukherjee, R. N. Jenjeti, and S. Sampath, "Active guests in the $MoS_2/MoSe_2$ host lattice: efficient hydrogen evolution using few-layer alloys of $MoS_{(2(1-x))}Se_{(2x)}$," *Nanoscale*, vol. 6, pp. 12856–12863, 2014.

[51] J. Jadczak, D. O. Dumcenco, Y. S. Huang, et al., "Composition dependent lattice dynamics in $MoS_xSe_{(2-x)}$ alloys," *J. Appl. Phys.*, vol. 116, p. 193505, 2014.

[52] H. Li, Q. Zhang, X. Duan, et al., "Lateral growth of composition graded atomic layer $MoS_{2(1-x)}Se_{2x}$ nanosheets," *J. Am. Chem. Soc.*, vol. 137, pp. 5284–5287, 2015.

[53] S. Hong, E. Kim, D.-W. Kim, T.-H. Sung, and K. No, "On measurement of optical band gap of chromium oxide films containing both amorphous and crystalline phases," *J. Non-Cryst. Solids*, vol. 221, pp. 245–254, 1997.

[54] F. Lou, R. Zhao, J. He, et al., "Nanosecond-pulsed, dual-wavelength, passively Q-switched ytterbium-doped bulk laser based on few-layer MoS_2 saturable absorber," *Photon. Res.*, vol. 3, p. A25, 2015.

[55] D. Mao, B. Du, D. Yang, et al., "Nonlinear saturable absorption of liquid-exfoliated molybdenum/tungsten ditelluride nanosheets," *Small*, vol. 12, pp. 1489–1497, 2016.

[56] Q. Bao, H. Zhang, Y. Wang, et al., "Atomic-layer graphene as a saturable absorber for ultrafast pulsed lasers," *Adv. Funct. Mater.*, vol. 19, pp. 3077–3083, 2009.

[57] X. Jiang, S. Liu, W. Liang, et al., "Broadband nonlinear photonics in few-layer MXene $Ti_3C_2T_x$(T = F, O, or OH)," *Laser Photon. Rev.*, vol. 12, p. 1700229, 2018.

[58] H. Zhang, J. He, Z. Wang, et al., "Dual-wavelength, passively Q-switched Tm:YAP laser with black phosphorus saturable absorber," *Opt. Mater. Express*, vol. 6, p. 2328, 2016.

[59] T. Wen, D. Zhang, Q. Wen, et al., "Enhanced optical modulation depth of terahertz waves by self-assembled monolayer of plasmonic gold nanoparticles," *Adv. Opt. Mater.*, vol. 4, pp. 1974–1980, 2016.

[60] Y. Sun, Y. Meng, H. Jiang, et al., "Dirac semimetal saturable absorber with actively tunable modulation depth," *Opt. Lett.*, vol. 44, pp. 582–585, 2019.

[61] B. Zhang, F. Lou, R. Zhao, et al., "Exfoliated layers of black phosphorus as saturable absorber for ultrafast solid-state laser," *Opt. Lett.*, vol. 40, pp. 3691–3694, 2015.

[62] G. J. Spühler, R. Paschotta, R. Fluck, et al., "Experimentally confirmed design guidelines for passively Q-switched microchip lasers using semiconductor saturable absorbers," *J. Opt. Soc. Am. B*, vol. 16, pp. 376–388, 1999.

[63] Y. Zhang, D. Lu, H. Yu, and H. Zhang, "Low-dimensional saturable absorbers in the visible spectral region," *Adv. Opt. Mater.*, vol. 7, p. 1800886, 2019.

[64] C. Hönninger, R. Paschotta, F. Morier-Genoud, M. Moser, and U. Keller, "Q-switching stability limits of continuous-wave passive mode locking," *J. Opt. Soc. Am. B*, vol. 16, pp. 46–56, 1999.